Interpretation of porosity and LWD resistivity from the Nankai accretionary wedge in light of clay physicochemical properties: Evidence for erosion and local overpressuring

Marianne Conin, P. Henry, S. Bourlange, Hugues Raimbourg, Thierry Reuschlé

Interpretation of porosity and LWD resistivity from the Nankai accretionary wedge in light of clay physicochemical properties: Evidence for erosion and local overpressuring

M. Conin
Université Aix–Marseille III, CEREGE, CRPG, Bat. Trocadero, Europole de l'Arbois, F-13545 Aix en Provence, France (conin@cdf.u-3mrs.fr)

P. Henry
CEREGE, CNRS, Europole de l'Arbois, BP 80, F-13545 Aix en Provence CEDEX 04, France

S. Bourlange
CRPG, CNRS, 15 rue Notre Dame des Pauvres, F-54501 Vandoeuvre-lès-Nancy, France

H. Raimbourg
Orleans University, CNRS, Château de La Source, Avenue du Parc Floral, BP 6749, F-45067 Orléans CEDEX 2, France

T. Reuschlé
Institut de Physique du Globe de Strasbourg, CNRS, 5 rue Rene Descartes, F-67084, Strasbourg, France

[1] In this study, we used porosity to assess the compaction state of the Nankai accretionary wedge sediments and any implications for stress and pore pressure. However, hydrous minerals affect porosity measurements, and accounting for them is essential toward defining the interstitial porosity truly representative of the compaction state. The water content of sediments was measured in core samples and estimated from logging data using a resistivity model for shale. We used the cation exchange capacity to correct the porosity data for the amount of water bound to clay minerals and to correct the porosity estimates for the surface conductivity of hydrous minerals. The results indicate that several apparent porosity anomalies are significantly reduced by this correction, implying that they are in part artifacts from hydrous minerals. The correction also improves the fit of porosity estimated from logging-while-drilling (LWD) resistivity data to porosity measured on cores. Low overall porosities at the toe of the accretionary wedge and in the splay fault area are best explained by erosion, and we estimated the quantity of sediments eroded within the splay fault area by comparing porosity-effective stress relationships of the sediments to a reference curve. Additionally, a comparison of LWD data with core data (resistivity and *P* wave velocity) obtained at Site C0001 landward of the mega-splay fault area, suggested a contribution from the fracture porosity to in situ properties on the formation.

Theme: Mechanics, Deformation, and Hydrologic Processes at Subduction Complexes, With Emphasis on the Nankai Trough Seismogenic Zone Experiment (NanTroSEIZE) Drilling Transect
Guest Editors: D. Saffer, P. Henry, and H. Tobin

1. Introduction

[2] Fluid and fluid overpressure zones are thought to play an important role on tectonic processes such as fault and décollement initiation and slip, and on the transition from seismic to aseismic behavior [e.g., *Hubbert and Rubey*, 1959; *Dahlen*, 1984; *Moore and Vrolijk*, 1992; *Le Pichon et al.*, 1993; *Saffer and Bekins*, 2006; *Scholz*, 1998; *Moore and Saffer*, 2001]. In accretionary complexes, porosity along with other physical properties of the sediment such as electrical resistivity and *P* wave velocities, are used as indicators of the effective stress supported by sediments [e.g., *Bangs et al.*, 1990; *Screaton et al.*, 2002; *Hart et al.*, 1995; *Gordon and Flemings*, 1998]. One approach consists in comparing porosity trend to a reference porosity-effective stress relationship defined from data acquired where the fluid pressure can be assumed hydrostatic and the compaction uniaxial [*Hart et al.*, 1995; *Screaton et al.*, 2002]. Excess pore pressure during loading slows or prevents consolidation, maintaining high porosity. Compressive tectonic stress applied under drained conditions results in a lower porosity for a given overburden [e.g., *Karig*, 1993] and may explain a generally higher porosity depth gradient within an accretionary wedge as compared with trench sediments [*Bray and Karig*, 1985]. Erosion yields sediments that have a lower porosity than anticipated from estimated in situ vertical effective stress, resulting in an apparent translation of the porosity-effective stress curve toward lower effective stress values. However, porosity measurements depend upon the lithology and the clay mineralogy, especially upon the water bound to hydrous minerals [e.g., *Brown and Ransom*, 1996]. In the case of Nankai, smectite is the dominant mineral that holds bound water interlayered between its silico-aluminate sheets [*Henry and Bourlange*, 2004; *Underwood and Steurer*, 2003]. This water should be considered as an intrinsic part of the mineral, as most of it is retained during compaction under the P and T conditions that prevail at this setting [*Brown and Ransom*, 1996; *Colten-Bradley*, 1987]. Therefore, porosity measurements should be corrected for smectite interlayered water.

[3] The main objective of this study is to identify anomalies of porosity within the sediments of the Nankai margin from boreholes drilled during IODP expeditions 314, 315, and 316 [*Kinoshita et al.*, 2009] (Figures 1 and 2) and to examine their relationship with tectonic and hydrologic processes. In order to take into account the effects of variations in clay mineralogy on porosity we propose the use of methods based upon previous work performed on Nankai and Barbados accretionary complex sediments [*Henry*, 1997; *Bourlange et al.*, 2003].

[4] In addition to porosity measured on cores, we estimate porosity from resistivity logging data set using a shale model that explicitly takes into account pore fluid composition, interlayer cation composition and temperature [*Revil et al.*, 1998]. One purpose of this estimation is that logging provides a continuous data set that allows an interpolation in zones where core recovery is poor, as well as some indication regarding the porosity evolution beyond the cored depths. Here, we show that the shale model utilized for estimating porosity from resistivity predicts the interstitial porosity better than the total porosity.

[5] We found that erosion in the splay fault area and at the toe of the accretionary wedge influenced the compaction state of the accretionary wedge, as well as the slope sediments. We estimated the amount of erosion at the top of the slope sediments in the splay fault area. We observed that the sediment underthrust below the splay fault appeared relatively less compacted, and we discuss possible causes for this phenomenon. We also use interstitial porosity estimates in order to highlight the probable zones of fluid overpressure within the accretionary wedge. We found that in the thrust sheet, above the main out of sequence thrust (splay fault), the discrepancy between resistivity and *P* wave velocity obtained on
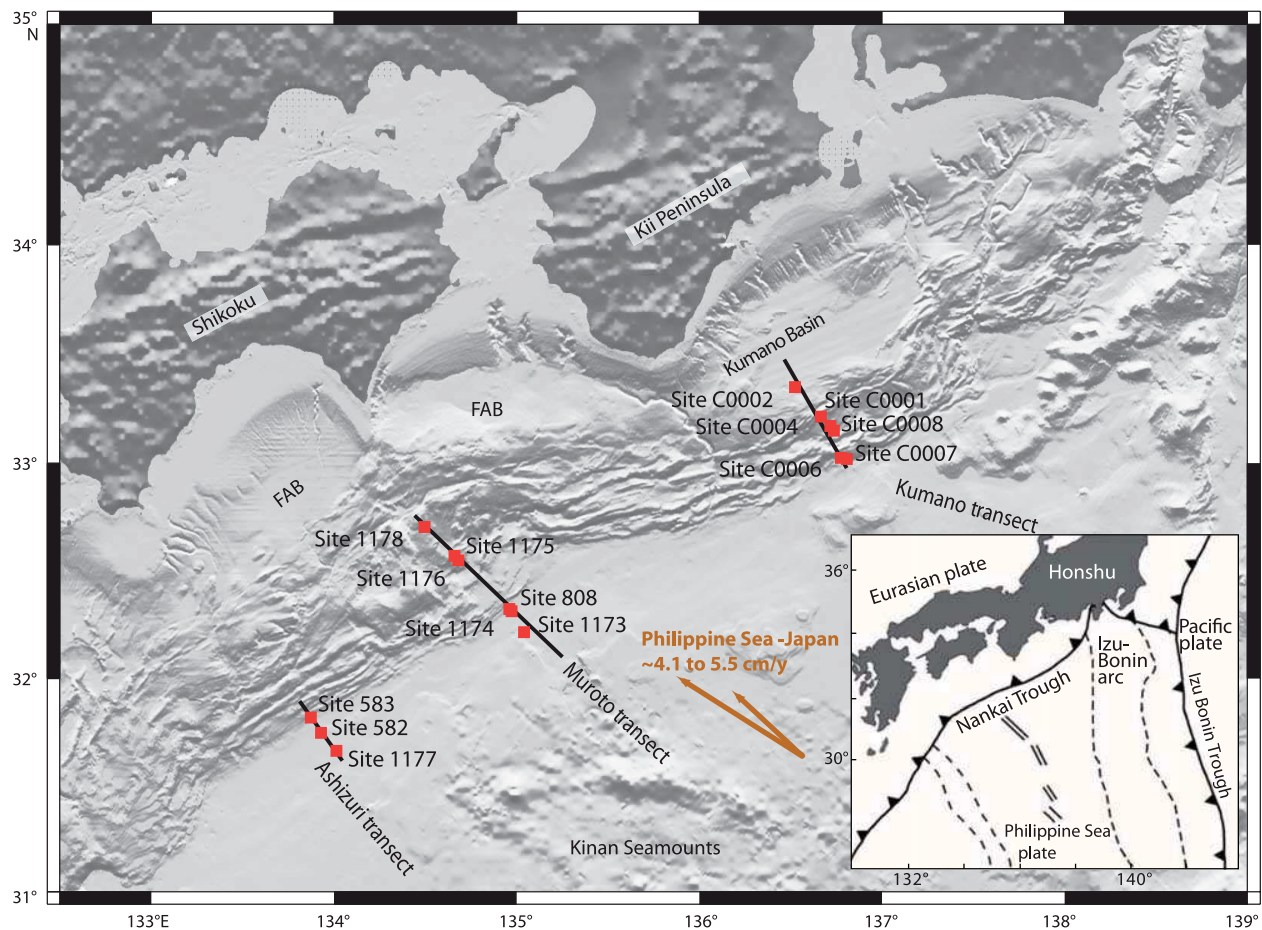
Figure 1. Regional bathymetry of southwest Japan, offshore the Kii Peninsula [*Moore et al.*, 2009], showing location of Nankai Trough and transects of Ashizuri (DSPD Leg 87 and ODP Leg 190), Muroto (ODP Legs 131, 190, and 196), and Kumano (IODP Legs 314, 315, and 316) [*Kinoshita et al.*, 2009]. Red dots correspond to drilled sites.

discrete samples and obtained on logging data is probably due to the presence of dilated fractures.

2. Geological Background, Drilled Site Locations, and Onboard Measurements

[6] The Nankai accretionary complex is formed by the subduction of the Philippine Sea plate, and the overlying Shikoku Basin, beneath the southwestern section of the Japan Arc (Figures 1 and 2). The study presented here focuses on logging-while-drilling (LWD) and core data obtained at five sites located along the Kumano transect (Figures 1 and 2) from the deformation front in the Nankai Trough to the Kumano fore-arc basin [*Kinoshita et al.*, 2009]. At this location the velocity of the downgoing plate with respect to the Japanese arc is estimated between 45 and 55 mm/yr [*Seno et al.*, 1993; *Henry et al.*, 2001; *Miyazaki and Heki*, 2001] along a N305–310° direction (Figure 1). Site C0006

is located at the toe of the accretionary wedge and penetrates a frontal thrust (Figures 2 and 3). Sites C0004, C0008, and C0001 are located in the mega splay fault zone [*Moore et al.*, 2009] (Figure 2). The mega splay is a system of Out Of Sequence Thrusts (OOST) located at the updip limit of the seismogenic zone and is thought to slip coseismically during large earthquakes [*Park et al.*, 2002]. Site C0004 crosses one of the OOSTs (Figures 2 and 3), which has accommodated at least 1.9 km of the horizontal throw since 1.95 Ma [*Strasser et al.*, 2009]. It was drilled into the slope apron and the accreted sediments in the hanging wall of this fault, and reached underthrust slope sediments. Site C0008 was drilled ~1 km seaward of site C0004 (Figures 2 and 3). It cored a complete stratigraphic section of the slope basin at the foot of this OOST down to the top of the accretionary prism. Site C0001 was drilled into a thinner slope apron and the accreted sediments in the hanging wall of the fault (Figures 2
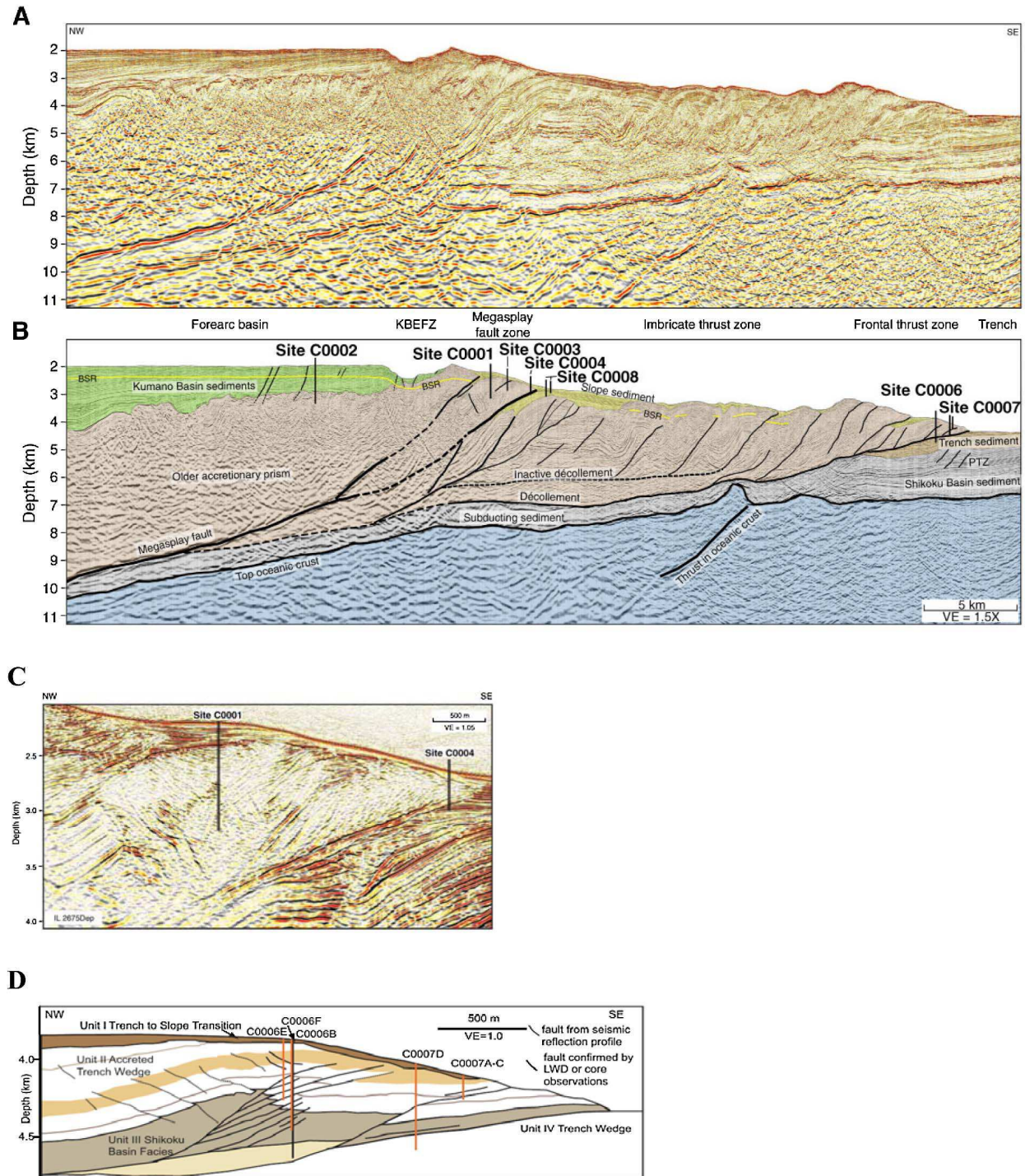
Figure 2. (a) Cross section of Kumano transect [from *Moore et al.*, 2009]. (b) Interpreted cross section of the Kumano transect. Sites drilled during IODP Expeditions 314, 315, and 316 are shown. The green shading indicates Kumano Basin sediments, and yellow shading indicates slope sediments. PTZ, protothrust zone; KBEFZ, Kumano Basin Edge Fault Zone [from *Moore et al.*, 2009]. (c) Detail of seismic profile crossing Sites C0001 and C0004 in the mega-splay fault zone. VE, vertical exaggeration (inline 2675) [*Moore et al.*, 2009]. (d) Interpretation of seismic profile crossing site C0006 at the toe of the wedge. VE, vertical exaggeration [*Screaton et al.*, 2009].

Figure 3

Figure 4. Cation exchange capacity (CEC, in mol kg^{-1}) versus normalized abundance of clay mineral content (wt %).

and 3). Site C0002 (Figures 2 and 3) penetrated the Kumano fore-arc basin near its seaward edge, and reaches the underlying accretionary complex [*Kinoshita et al.*, 2009]. All of the boreholes are shallower than 1500 m below seafloor.

[7] Five categories of facies are found [*Kinoshita et al.*, 2009] (Figure 3): (1) the slope apron mainly composed of silty clay to clayey silt hemipelagites and volcanic ash, (2) accreted sediments composed of fine-grain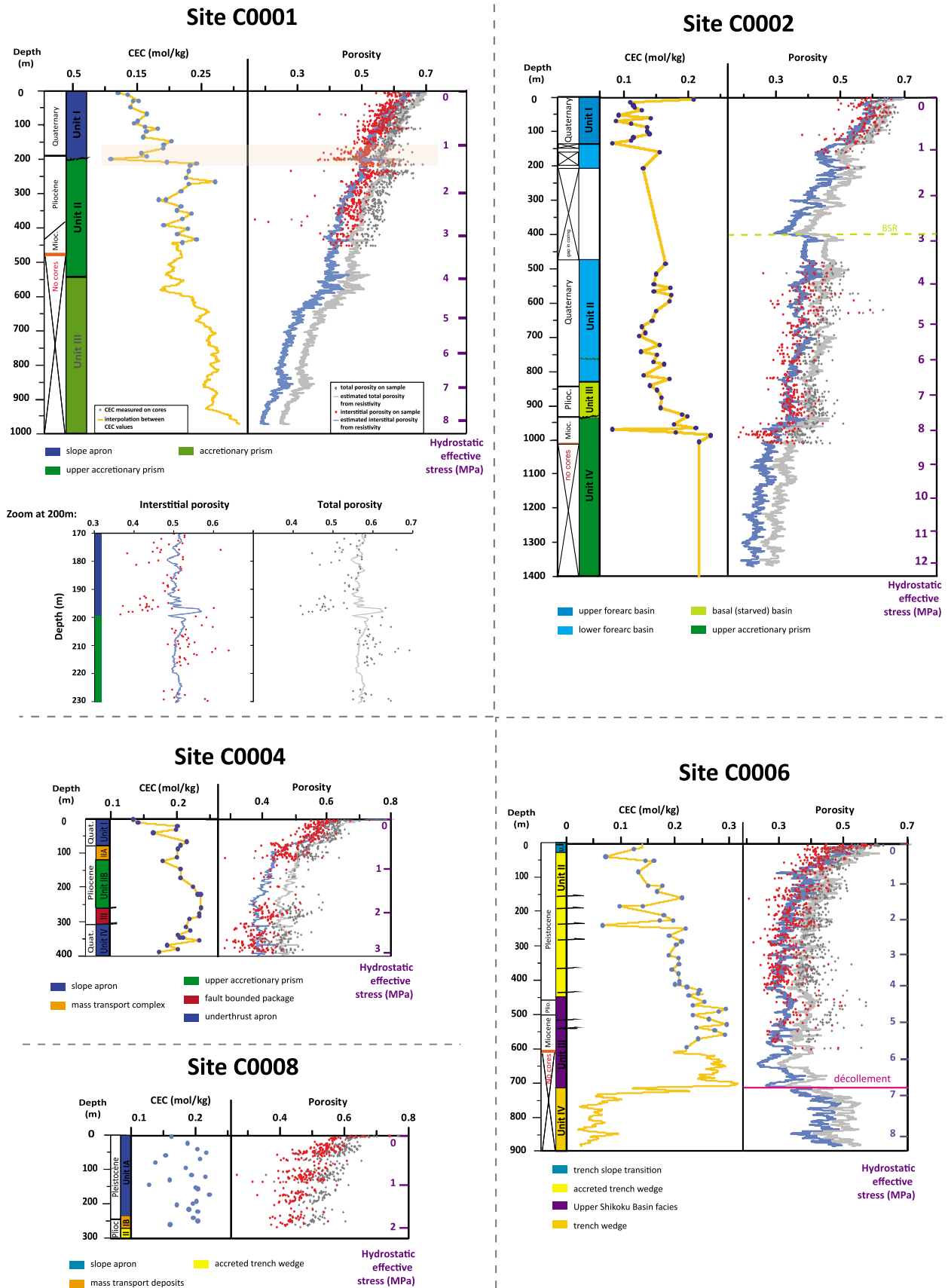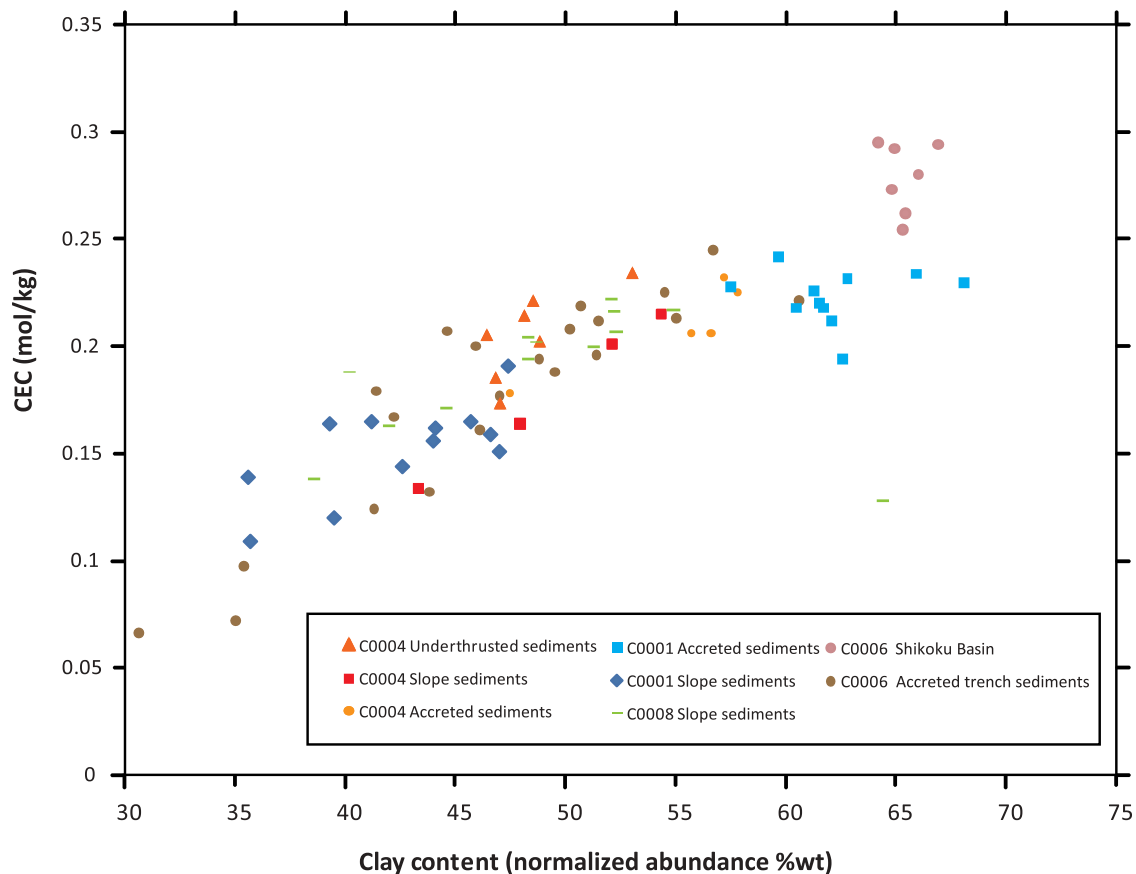ed terrigenous material and hemipelagites, (3) Kumano fore-arc basin sediments mainly composed of sandy turbidites and hemipelagic mud, (4) trench sediments composed of silt, sand- and gravel-bearing turbidites and muddy marine sediments, and (5) the Upper Shikoku Basin

composed of silty clay to clayey silt hemipelagites and volcanic ash. A weak cementation may be present in this facies [*Kinoshita et al.*, 2009], and in the accreted sediments of Site C0001, at least in the cored interval (down to ~450 m), [*Hashimoto et al.*, 2010; *Raimbourg et al.*, 2011], but it is absent at the other sites [*Raimbourg et al.*, 2011].

[8] Overall, the XRD analysis at the Kumano transect [*Kinoshita et al.*, 2009] indicates that the clay mineral content (relative to silt) increases from the hemipelagic mud of the Kumano fore-arc basin, to slope sediments, to accreted trench sediments, and then to accreted sediments and Upper Shikoku Basin sediments (Figure 4). The results from ODP

Figure 3. Lithology, cationic exchange capacity (CEC) content (in mol kg^{-1}), and total and interstitial porosity at Sites C0002, C0001, C0004, C0008, and C0006 versus depth and excess lithostatic stress. For CEC content, blue dots are measured in laboratory on discrete samples, and orange line is interpolated from those values. For porosity, dark dots correspond to total porosity measured on discrete samples, and reds dots correspond to interstitial porosity calculated from total porosity and CEC measurements on discrete samples. Grey and blue lines correspond to porosity estimated from bit resistivity measurements fitted on total and interstitial porosity, respectively. The stepwise increase of the LWD resistivity measurements observed at ~400 m below sea level at Site C0002 coincides with a gas hydrate bottom simulating reflector. At Sites C0001 and C0006, CEC content is derived from gamma ray log (see text) below 450 m and below 590 m, respectively.
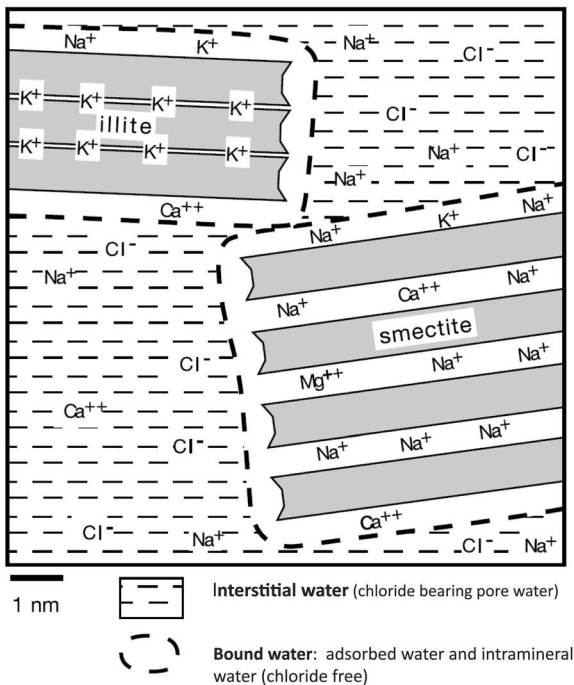
Figure 5. Distribution of water and ions in clay rich material [modified from *Henry and Bourlange*, 2004].

drilling Leg 131, 190 and 196 located in the Muroto transect (Figure 1) and from IODP expeditions 315 and 316 located in the Kumano transect (Figure 1) indicated that an important proportion of the clay minerals present within the Nankai sediments is smectites [*Henry and Bourlange*, 2004; *Underwood and Steurer*, 2003; *Kinoshita et al.*, 2009], and that smectite interlayered water can be present at levels up to 25% of the total volume of water [*Henry and Bourlange*, 2004].

[9] In water-saturated sediments 'total porosity' is defined in laboratory measurements as the ratio between the total volume of water removed by oven drying at 105°C and the wet sample volume. When sediments are rich in hydrous minerals such as smectites, zeolites, and gypsum, this definition of porosity includes the water contained in the minerals and the water adsorbed on the external surfaces of the minerals. In the following discussion, the volume of water present in the pore space is referred to as the 'interstitial porosity' while the water in the minerals and adsorbed on the surfaces of the minerals is referred to as the 'bound water'. The total porosity (ϕ_t) was measured on discrete core samples on board the *D/V Chikyu* by IODP expeditions 315 and 316 scientists [*Kinoshita et al.*, 2009]. A detailed description of the methods can be

found in the work of *Blum* [1997]. The porosity measurements (black dots on Figure 3) show substantial variations across lithological boundaries [*Kinoshita et al.*, 2009]. This is the case at Site C0001 between the slope apron and the accreted sediments, at Site C0006 between the accreted trench wedge and the Upper Shikoku Basin, and at Site C0004 between the slope apron and the accreted sediments. We also observed that the porosity of the accreted sediments at site C0004 is lower than for similar sediments at Site C0001 (black dots on Figure 3) and that the porosity of silty trench sediments at Site C0006 is low (0.35 at 300 m) compared to the porosity at the other sites.

3. Method

3.1. Interstitial Porosity Determination on Core Samples

[10] Porosity measurements performed on the cores using standard methods [*Blum*, 1997] reflect the total water content present within the sediments including the water contained in hydrous minerals, which primarily refers to smectites in the case of the Nankai sediments [*Henry and Bourlange*, 2004; *Underwood and Steurer*, 2003]. Previous researches proposed correction for bound water based on smectite content determinations obtained using XRD [*Brown and Ransom*, 1996; *Hashimoto et al.*, 2010]. We propose a correction based upon cation exchange capacity (CEC) determinations and apply it to shipboard porosity measurements on cores in order to calculate the interstitial porosity.

[11] Illite and smectite clay mineral layers are negatively charged (Figure 5). In a saline fluid this charge is compensated by the presence of hydrated cations (Na^+, K^+, Ca^{2+}, and Mg^{2+}) in the interlayer spaces, and is adsorbed on external clay surfaces [e.g., *Clavier et al.*, 1984]. In theory, each cation charge present in a hydrated smectite interlayer is associated with 15 water molecules [*Ransom and Helgeson*, 1994], but this number may depend upon the layer charge and the interlayer cation composition. Therefore, the bound water content in sediments rich in smectite and illite can be calculated using the CEC (in mol kg^{-1} of dried sample) [*Clavier et al.*, 1984; *Henry*, 1997; *Henry and Bourlange*, 2004] and the interstitial porosity (ϕ_i) expressed as a function of the total porosity (ϕ_t), the CEC in mole per kilogram of dried sample, the water molar mass (m_w) (0.018 kg mol^{-1}), the water density (ρ_w) (1024 kg m^{-3}), the grain density (2650 kg m^{-3}) (ρ_g),
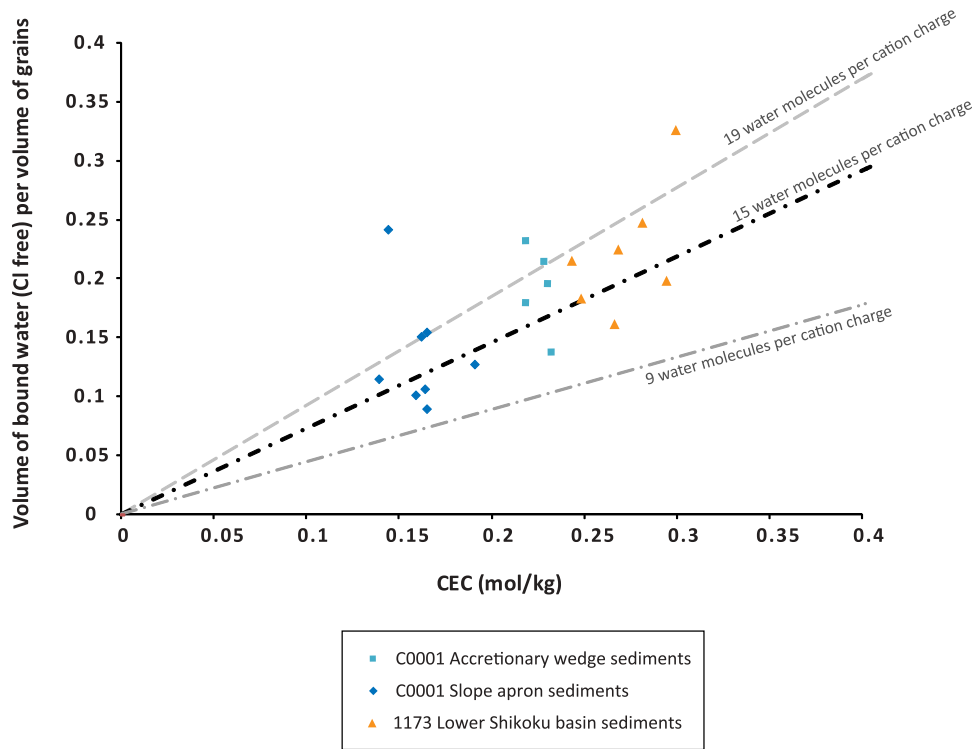
Figure 6. Bound water volume (chloride free) per volume of grain (bound water ratio) versus cation exchange capacity (CEC) on samples from IODP Expeditions 315, Site C0001 (in blue), and ODP Expedition 190, Site 1173 (in orange). Lower Shikoku Basin facies corresponds to hemipelagites [*Moore et al.*, 2001]. Lines correspond to 9, 15, and 19 water molecules per cation charge.

and the average number of water molecules per cation charge (n), as follows:

$$\phi_i = \phi_t - n* \frac{m_w}{\rho_w} \cdot CEC. \, \rho_g \cdot (1 - \phi_t). \qquad (1)$$

The CEC utilized in this study (as for in previous work done on Nankai and Barbados ODP samples by *Henry* [1997] and *Henry and Bourlange* [2004]) was measured by exchanging the cations with cobaltihexamine chloride [*Orsini and Remy*, 1976]. All of the measurements were made at the Institut National de Recherche Agronomique (INRA) soil analysis laboratory at Arras.

[12] The value of n may be estimated experimentally using the budget of water and chloride contained in the sample [*Henry and Bourlange*, 2004] where the bound water is assumed chloride free while the chlorinity of the interstitial water is approximately known from the composition of pore water extracted in a press and analyzed on board during IODP expeditions 315 and 316 [*Kinoshita et al.*, 2009]. Previous studies performed on Nankai and Barbados accretionary wedge samples concluded that the sediments retain, in average, 12

bound water molecules per cation charge after pore fluid extraction on board but that three or four of the bound water molecules are removed during the squeezing process [*Henry and Bourlange*, 2004]. We compared the bound water content of samples from Site 1173 [*Henry and Bourlange*, 2004] and Site C0001 and found that a value of 15, as theoretically suggested [*Ransom and Helgeson*, 1994], is compatible with the data. However, depending upon the samples analyzed, the data may reflect a wide range of variation (Figure 6).

3.2. Computation of Porosities From Logging-While-Drilling Data

[13] Using logging data, the total porosity can be measured with neutron porosity (with a known or assumed water saturation) or calculated from density measurements if fluid and grain densities are known or assumed. Alternatively, the resistivity and the P waves velocity can be calibrated either theoretically or empirically and used as a proxy for porosity. Density and neutron porosity measurements are only available at Site C0002 and from the first 450 m at Site C0001 [*Kinoshita et al.*, 2009],

and both types of measurements are strongly affected by borehole conditions. The LWD resistivity is less affected by borehole conditions, and the data quality was assessed using resistivity imaging data [*Chang et al.*, 2010]. Here, we rely upon the resistivity at the bit, which has a larger investigation depth and, conversely, a lower resolution but is the least sensitive to borehole conditions.

[14] We estimate porosity from the resistivity logging data using a shale model which takes into account clay surface conductivity [*Bourlange et al.*, 2003; *Revil et al.*, 1998]. One purpose of this estimation is that logging provides a continuous data set that allows interpolation in zones where the core recovery is poor, as well as some indication regarding the porosity evolution beyond the cored depths (in C0001 and C0006). The model is also important for the assessment of the interstitial porosity concept.

[15] The resistivity model is based upon the Hanai-Bruggeman equation which relates the electrical properties of a heterogeneous mixture to the properties of individual components [*Bussian*, 1983]. The approach was further developed by *Bussian* [1983] and *Revil et al.* [1998] in order to take into account the temperature dependency and the exchangeable cation composition. We use an approximate relationship derived from a Taylor expansion at high salinity [*Bourlange et al.*, 2003] between the bulk conductivity of the sediments (σ_b), the interstitial fluid conductivity (σ_{if}), the surface conductivity of clay particles (σ_s), and the porosity (the porous medium is assumed to be water saturated), as follows:

$$\sigma_b = \sigma_{if}\phi^m\left[1 + 2*\frac{\sigma_s}{\sigma_{if}}\left(\frac{\sigma_{if}}{\sigma_b} - 1\right)\right]. \qquad (2)$$

[16] The formation factor, *F*, is defined as the limit of σ_{if}/σ_b for a zero surface conductivity and follows the classical Archie's law [*Archie*, 1942]:

$$\frac{1}{F} = \underset{\sigma_r \to 0}{Lim}\frac{\sigma_b}{\sigma_{if}} = \frac{\phi^m}{a}, \qquad (3)$$

where *a* and *m* are empirically derived constants. Here *m* typically ranges from 1 to 3.5, and *a* is here equal to 1. Assuming here a constant *a* distinct from 1 would not be theoretically consistent since the formation factor should tend to 1 for a porosity of 1 [*Glover et al.*, 2000; *Bussian*, 1983].

[17] Interstitial fluid conductivity is calculated from the major element composition determined on board

(see the auxiliary material).[1] The clay surface conductivity is calculated from the cation exchange capacity and the cation composition (see the auxiliary material). The analytical expressions appear by *Revil et al.* [1998] and *Bourlange et al.* [2003] and are also provided in the auxiliary material. In order to perform the calculations at all depths where the logging resistivity (or the sample porosities) were acquired, we linearly interpolated the CEC, the exchangeable cation composition, and interstitial fluid conductivity values between measurements.

[18] Natural gamma ray is frequently used as a proxy for clay content, and at Sites C0006 and C0001 a certain correlation exists between LWD gamma ray (GR) and CEC measurements (see the auxiliary material), which can be fitted using a linear regression, as follows:

$$CEC_{proxy} = 0.038 \times GR - 0.0616. \qquad (4)$$

Gamma ray data is mainly sensitive to the bulk K (potassium) content, and therefore to the illite content while bound water and surface conductivity variations are determined by smectite, which has a minimal amount of K. Therefore the CEC may correlate with gamma ray only if the mineralogical composition of the clay fraction is constant, such that CEC variations only reflect variations in the total clay content. For this reason, we only used this proxy in order to extrapolate the CEC below the coring depth at Sites C0001 and Sites C0006 (Figure 3) where no other data were available.

[19] Equation (2) could then be rewritten in an explicit form in order to compute the porosity estimate from the available data, as follows:

$$\phi = \left[\frac{\sigma_{if}}{\sigma_b}\left[1 + 2*\frac{\sigma_s}{\sigma_{if}}\left(\frac{\sigma_{if}}{\sigma_b} - 1\right)\right]\right]^{-1/m}. \qquad (5)$$

[20] An important unknown is the meaning of the porosity term in the equation (whether it is the interstitial porosity or the total porosity). Under a high-salinity domain, the charge of the smectite clay layers is balanced by the interlayer cations and the ions adsorbed on external surfaces (the Stern layer). The conductivity is dominated by the movement of these cations along the Stern layer and likely in the interlayer spaces [*Leroy and Revil*, 2004; *Revil et al.*, 1998; *Bussian*, 1983]. Therefore, surface conductivity takes place in a volume of bound water,

Table 1. Resistivity Model Parameters Used to Estimate Porosity From Resistivity and Corresponding Correlation Coefficient Between Samples and LWD Data, for Model Fitted on Interstitial Porosity and Fitted on Total Porosity Data Set

| Holes | Numbers of Samples | Archie's Law Parameters $a = 1$; m | | Correlation Coefficient Between Sample Porosity and Porosity Estimated From LWD | |
		Total Porosity	Interstitial Porosity	Total Porosity	Interstitial Porosity
C0002	489	2.3	2.0	0.90	0.91
C0001	603	2.5	2.1	0.63	0.73
C0004	360	2.4	2.0	0.84	0.86
C0008	284	–	–	–	–
C0006	564	2.1	1.7	0.68	0.77

from which anions are mostly excluded. The consistency of the model implies that the limit case in equation (5) must be taken at a constant geometry. This can be achieved mathematically by considering a virtual case in which the mobility of adsorbed and interlayer ions tends to zero without a modification of the distribution between the bound and interstitial water or the density distribution of the ions. At the limit, interstitial water is the only conductive medium. By assuming that a granular medium with nonconducting grains will follow Archie's law, an assertion supported by numerical works that have simulated electrical conduction in densely packed of insulating spheres saturated by a conductive phase [e.g., *Sen and Kan*, 1987], it follows that the porosity in equation (5) should be the interstitial porosity rather that the total porosity.

[21] Again, this leads to consider water bound to clay particles as an intrinsic part of the clay particle and to logically infer interstitial porosity rather than total porosity from the logs:

$$\phi_i = \left[\frac{\sigma_{if}}{\sigma_b}\left[1 + 2*\frac{\sigma_s}{\sigma_{if}}\left(\frac{\sigma_{if}}{\sigma_b} - 1\right)\right]\right]^{-1/m_i}. \quad (6)$$

The only adjustable parameter in equations (5) and (6) is the cementation exponent (m and m_i, respectively); m is determined by fitting porosity estimations from resistivity on total porosity measurements on core samples, and m_i is determined by fitting the porosity estimation from resistivity on the calculated interstitial porosity. The interstitial porosity is obviously, smaller than the total porosity, and m_i is systematically lower than m. We computed the correlation coefficient of the fit and found that it is higher for the interstitial porosity model than for the total porosity model (Table 1).

3.3. Compaction Curves

[22] At geological depth and pressure, the relation between porosity (ϕ) versus effective stress (σ') is

assumed to be exponential [e.g., *Rubey and Hubbert*, 1959]:

$$\phi(\sigma') = \phi_0 \times \exp[-\alpha \times \sigma'], \quad (7)$$

where α is an empirical compaction coefficient and ϕ_0 is the initial interstitial porosity. In rocks, the total stress, σ_t, is partitioned between the pore fluid pressure, P, and the effective stress, σ', carried by the matrix, as follows:

$$\sigma_t = \sigma' + P. \quad (8)$$

[23] The pore fluid pressure is equal to the sum of the excess pore pressure, P^*, and the hydrostatic pressure P_H:

$$P = P^* + P_H. \quad (9)$$

If the compaction of the sediments is essentially vertical, σ_t is assumed to be equal to the lithostatic pressure, σ_L, and equation (8) can be rewritten as follows:

$$\sigma_L = \sigma' + P. \quad (10)$$

[24] When substracting the hydrostatic pressure, P_H, we obtain the following:

$$\sigma_L^* = \sigma' + P^* \quad \text{or} \quad \sigma' = \sigma_L^* - P^*, \quad (11)$$

where σ_L^* is the excess lithostatic pressure. Under conditions of hydrostatic pore pressure (P^* equals zero), the effective stress equals the effective lithostatic pressure, $\sigma' = \sigma_L^*$ which allowed us to establish the porosity versus effective stress relationship. The relationship can be used as a reference for a given lithology, to which other porosity curves can be compared.

[25] The lithostatic pressure is calculated by integrating bulk density data measured on core samples. Where no density log or density data on cores were available, we calculated bulk density data from the
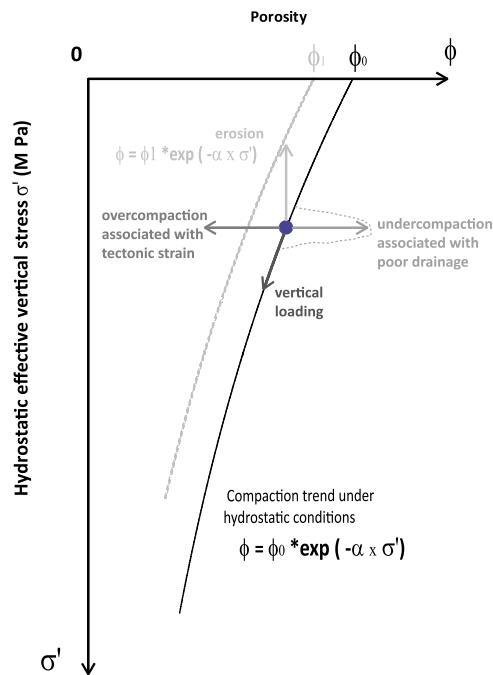
Figure 7. Cartoon explaining theoretical shift of porosity due to tectonic or hydrologic processes.

porosity estimated from resistivity logs. The bulk density (ρ_b) is calculated as follows:

$$\rho_b = \phi \times (\rho_w - \rho_g) + \rho_g, \qquad (12)$$

where ϕ is the porosity, ρ_b is the bulk density, ρ_w is the water density (1024 kg/m³) and ρ_g is the grain density (2650 kg/m³). In slope sediments at the top of Site C0001 the structural data on the cores and the resistivity images show no evidence of tectonic compression [*Kinoshita et al.*, 2009]. Additionally, the low sedimentation rate for those sediments [*Kinoshita et al.*, 2009] and results from consolidation tests [*Song et al.*, 2008] indicate that the pore pressure is likely hydrostatic. Thus, we assume that the porosity curve of these sediments, as a function of effective stress, can be used as a reference curve. Deviation of interstitial porosity from the reference curve can be interpreted in terms of tectonic or hydrologic processes (Figure 7). Compaction disequilibrium and poorly drained loading leads to excess pore pressure and undercompaction, while compressive tectonic stress leads to overcompaction. Erosion results in anomalously low porosity for a given present-day depth; the effect is that the porosity curve appears offset to shallower depth (lower effective stress). In order to quantify the total amount of erosion, porosity curves

are offset until they match the reference compaction curve. A best fitting offset is determined using the least square method. In the accretionary wedge, where compaction is certainly not uniaxial, comparison of compaction trends along a transect also provide information regarding spatial variations of tectonic stress, fluid pressure and stress paths (e.g., unloading due to erosion). Variations resulting from combined effects cannot be resolved.

4. Results and Implications

4.1. CEC and Lithology

[26] All of the cation exchange capacity measurements made on core samples range between 0.05 to 0.35 mol kg⁻¹. The CEC values, as well as their range of variation is smaller for the Nantroseize transect than at the sites previously drilled on the Muroto and Ashizuri transects [*Underwood and Steurer*, 2003; *Henry and Bourlange*, 2004] (Figure 1). However, substantial variations in the CEC content are observed across lithological boundaries (Figure 3), especially at Site C0001 between the slope apron and the accreted sediments (Figures 3 and 4). These variations correlates well with variations in total clay content (Figure 4), and we expect a stronger correlation with smectite content (M. B. Underwood et al., manuscript in preparation, 2011). The maximum temperatures in all boreholes are lower than 45°C [*Kinoshita et al.*, 2009], implying that the smectite/illite reaction is not occurring. Therefore, variations in the CEC must result primarily from differences in detrital clay. Variations of volcanic input and low-temperature alterations of ash may be other factors that influence clay content swelling and the CEC.

4.2. Porosity Corrections

[27] In the transition at Site C0001 from slope sediments to accreted sediments at ~200 m (Figure 3), total porosity on samples increases by 11% while interstitial porosity only increase by 5%. Porosity estimations from resistivity log display an even smaller increase (<3%). We assumed, based on theoretical reasoning, that the resistivity model yielded a proxy for the interstitial porosity rather than the total porosity. While still not ideal, the behavior of the proxy across this lithological boundary is closer to that of the interstitial porosity (than the total porosity). We have seen that this lithological boundary corresponds to an increase of the clay content within the accreted sediments, and
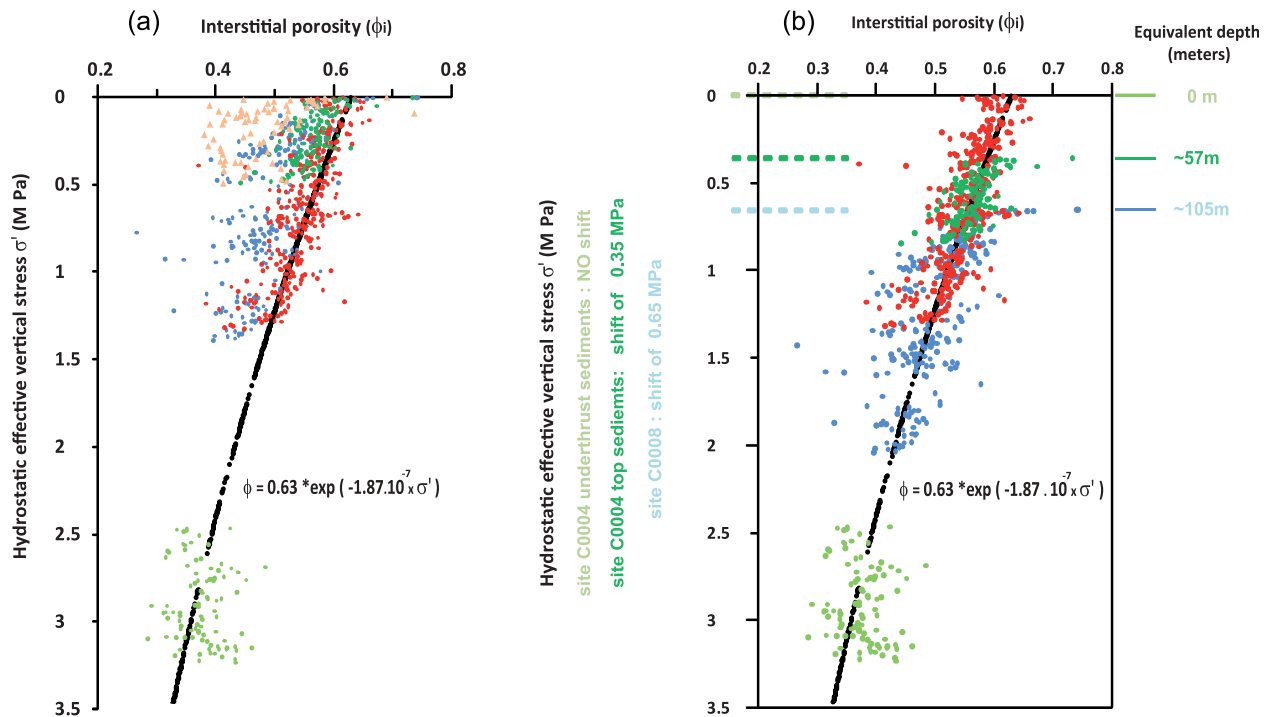
Figure 8. (a) Interstitial porosity estimated from discrete samples versus excess lithostatic stress for slopes sediments at Sites C0001 (red), C0004 (green), C0008 (blue), and C0006 (purple) and for underthrust sediments at Site C0004 (light green). Sediments at Site C0001 are used to define a reference porosity-effective stress curve (in black, with corresponding equation). (b) Interstitial porosity versus excess lithostatic stress for samples from slope apron sediments of Sites C0001 (in red), C0004 (in green), and C0008 (in blue). Sediments at Site C0001 are used to define a reference porosity-effective stress curve (in black, with corresponding equation). To quantify erosion, slope and underthrust sediments of Site C0004 and Site C0008 are stress shifted to fit the reference compaction curve (an equivalence in meter is also given). Shifts are determined using the least square method.

to a proportional increase in CEC. We find that taking into account bound water reduces the contrast in porosity across the lithological boundary (see zoom of Site C0001 in Figure 3). We observe similar patterns for the transition from slope sediment to accretionary wedge at Site C0004 and for the transition from Shikoku Basin hemipelagites to trench turbidites at Site C0006. However, a residual increase of porosity is still observed at the transition zone. This can be explained because the bound water correction only account in part for the general increase of the water content with clay content in clay-silt of clay-silt-sand mixtures. Conversely, the interstitial porosity of sediments with different textures and compositions will still be different under the same stress conditions. At the transition zone of Site C0001, the residual increase could be related to a weak cementation of the accreted sediments. Such a cementation would also explain the observed lower fit of porosity estimated from resistivity model on samples data in the accreted sediments at this site (Figure 3), if cementation increases the resistivity values.

4.3. Compaction of the Sediments

4.3.1. Evidence and Quantification of Erosion at Sites C0004 and C0008

[28] The slope apron sediments at Sites C0004 and C0008 are more compacted than the reference slope sediments at Site C0001 (Figure 8a). Porosity versus effective stress curves for Sites C0008 and C0004 match the reference curve if the effective stresses are shifted by 0.65 MPa and 0.35 MPa, respectively. Since no evidence of compressive tectonic stress was found on cores of shallow sediments at Sites C0004 and C0008, the deviation of porosity from reference curves is likely to result from erosional unloading. Shifts of 0.65 MPa and 0.35 MPa would correspond to ~105 m and ~57 m of erosion, respectively (Figure 8b). These estimations are consistent with constraints from biostratigraphy and paleomagnetism [*Kinoshita et al.*, 2009] and comparable to estimations of the minimum thickness of material, ~90 m and ~40 m, respectively, that must
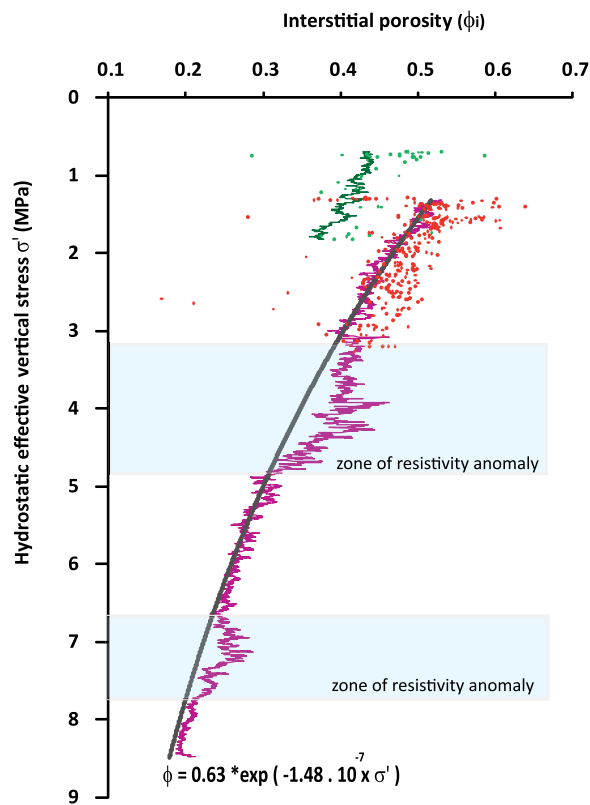
Figure 9. Interstitial porosity estimated from resistivity curves, and interstitial porosity of discrete samples versus excess lithostatic stress for accreted sediments at Sites C0001 (red) and C0004 (green).

have been eroded in order to form the scars observed in the bathymetry (M. Strasser et al., Slumping and mass-movement deposition in the Nankai fore arc: Evidence from IODP drilling and 3-D reflection seismic data, submitted to *Geochemistry, Geophysics, Geosystems*, 2010). Steps in the depth-age curves suggests that one or several episodes of slope erosion occurred between 1 and 0.4 Ma at Sites C0008 and C0004 (Strasser et al., submitted manuscript, 2010). At Site C0006 the low porosity of the slope sediments as compared to that of Site C0001 (Figure 8a) also suggests recent removal of material. However, the sequence is not thick enough to quantify erosion using a porosity-effective stress curve. Observations of truncation of sedimentary horizons in a seismic line at the toe of the prism [*Screaton et al.*, 2009] (Figure 2d), and the age versus depth curve obtained from biostratigraphy data [*Kinoshita et al.*, 2009] indicate that a major erosion also occurred at the top of the accreted trench sediments (~300 m). Such erosion could partly explain the overall low porosity of those sediments.

4.3.2. Compaction Below the Major Faults

[29] At Site C0004 seismic data and age data determined from coring show that the underthrust sediments below the fault bounded package (~305 m in Figure 3) are slope apron [*Kinoshita et al.*, 2009]. The age control on cores at Sites C0004 and C0008 indicates that their deposition (~1.7 to 1.5 Ma) is contemporaneous to an important phase of activity of the splay fault (estimate horizontal throw rates of 1.93 m kyr^{-1} between 1.7 and 1.55 Myr) [*Strasser et al.*, 2009], and occurred prior to erosion at the top of the slope sediments. However, the porosity of the sediments fit the reference curve without being shifted (Figure 8a). Unless the extrapolation of the reference curve at a greater effective stress is incorrect, the underthrusting sediment appears to be normally consolidated while it should be overconsolidated due to recent (>1 Ma) erosion, as observed in slope sediments at the same location. This may be explained if erosion unloading is compensated by thrusting along the splay fault, or if the footwall is overpressured. Since the recent (<1 Ma) rate of thrusting along the splay fault appears very low [*Strasser et al.*, 2009] and the erosion postdates 1 Ma, the most likely explanation is that the sediment was loaded by thrusting under poorly drained condition, such that footwall overpressuring during splay fault activity maintained the underthrust sediments in an undercompacted state relative to the reference curve. Then erosion occurred at the top of the section, and was followed by drainage of the underthrust sediments.

[30] At Site C0006, below the frontal thrust at 730 m, underthrusted trench sediments were identified [*Kinoshita et al.*, 2009], and comparatively, they had high estimated porosity values (40%–50%). The very low gamma ray [*Kinoshita et al.*, 2009] indicates a sand dominated lithology consistent with such a porosity. Here, the high porosity likely reflects a sandier, lower compressibility sediment framework rather than variations or anomalies in the effective stress.

4.3.3. Accreted Sediments

[31] No reference curve can be defined for the accreted sediments at Sites C0001 or C0004 since they are tectonically deformed [*Kinoshita et al.*, 2009]. However, the porosity of the sediments at Site C0004 is lower than the porosity of comparable accreted sediments at Site C0001 (Figure 9). A shift of ~1.5 MPa of the porosity versus effective stress curve of accreted sediments at Site C0004 is
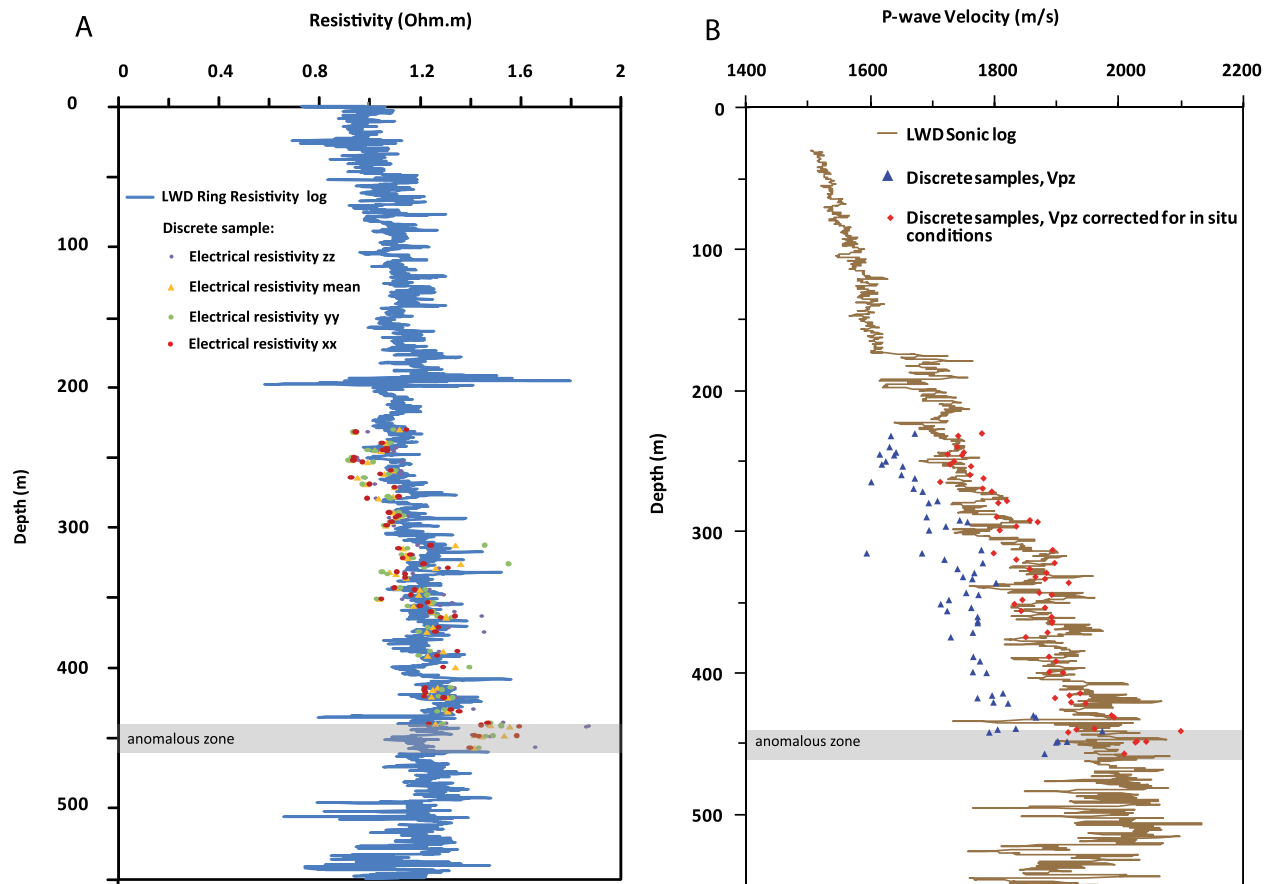
Figure 10. (a) Ring resistivity measurements from logging-while-drilling (LWD) and electrical resistivities in three directions (z, y, x) from discrete measurements versus depth. Electrical resistivity is calculated from electrical conductivity measured in laboratory and corrected for in situ temperature conditions (see text). (b) *P* wave velocity in vertical direction (*VP*z) from LWD and from discrete samples versus depth. Values in blue were measured in the laboratory. Values in red are the same measurements corrected for in situ conditions (see text).

necessary in order to match the two curves. The value is higher than the shift needed to correct the effect of erosion of the slope sediments at Site C0004. The weak cementation of accreted sediments at Site C0001, and possible lithological variations between the accreted sediments at the two sites could partly explain the difference of ~1.1 MPa between the two values. The difference could also be explained if accreted sediments at Site C0004 had undergone higher tectonic stress, or if they had been exhumed by hanging wall erosion that occurred during earlier stages of out-of-sequence thrusting activity (Figure 2c), notably during the age gap observed across the wedge-slope sediments unconformity [*Kinoshita et al.*, 2009]. The last hypothesis is consistent with the observations of Strasser et al. (submitted manuscript, 2010), who concluded that slope failures and mass transport complex formation

at the top of the accreted sediments are time-correlative to a high activity phase of thrusting activity, between 1.95 Ma to 1.8 Ma.

[32] At Site C0001, the resistivity is anomalously low in two zones at ~460 m and ~830 m (Figure 10). The zones include high-angle and vertical conductive fractures observed on the resistivity image [*Kinoshita et al.*, 2009]. Therefore, the increase in conductivity in the Resistivity at Bit (RAB) data may be explained (at least in part) by the presence of dilated fractures. Excursions in the estimated porosity reflect a decrease of resistivity, but are not quantitatively correct since the impact of fractures is not properly modeled using the shale resistivity model. At the top of this zone, at ~435 m, onboard scientists [*Kinoshita et al.*, 2009] observed that the in situ LWD resistivity and *P* wave velocity values

were lower than those on discrete samples after a correction for in situ conditions, and proposed that it could be due to the presence of dilated fractures and/or nonhydrostatic pore pressure. Since there is no lithologic change at that depth, the discrepancy between the sample and the LWD data could either result from a degradation of the borehole or from performing measurements at a different scale and/or under different conditions. At ~435–460 m, caliper data indicate that the borehole condition is still good, and that the drilling mud pressure is hydrostatic [*Kinoshita et al.*, 2009]. Resistivity of the samples corrected for variations of interstitial fluid conductivity with temperature follow the trend of the LWD data down to the top of the first anomalous zone (down to ~430 m). Further down, logging resistivity decreases, while that measured on the samples increases (between ~435 and ~460 m). Shipboard *P* wave velocities were corrected empirically by a fit of log data, which was not fully satisfactory for confinement [*Kinoshita et al.*, 2009]. A *P* wave velocity correction based upon shore-based *P* wave measurements was subsequently performed on samples from the accretionary wedge lithological unit at Site C0001 for confining pressures ranging from 3 to 30 MPa [*Raimbourg et al.*, 2011]. Assuming hydrostatic pore pressure conditions, the following correction is proposed (see auxiliary material):

$$V_p(corrected) = V_p(shipboard) + 10 \times \sigma' + 50 + 1.7 \times z' \times \rho_w \times g, \qquad (13)$$

where, z' is the depth in meters below sea level, ρ_w is the water density (1024 kg/m³) and g is the gravitational constant (9.8 m s⁻¹). After applying this correction, the *P* wave velocity data on the samples fit the LWD data from 230 to 430 m (Figure 10) and a deviation is still observed for the bottom samples, at ~435–460 m. Both the resistivity and the *P* wave LWD data are lower than the corrected discrete sample measurements. This indicates the presence of dilated fractures, a non-hydrostatic pore pressure, or a combination of both. The observation of numerous seismic reflections in the first zone is consistent with either explanation (Figure 2c) [*Moore et al.*, 2009]. However, because resistivity is primarily sensitive to effective pressure variations through porosity changes, fractures most likely account for the discrepancy in resistivity LWD and sample data. The minimum fracture porosity ϕ_c, associated with an in situ increase in conductivity, is estimated assuming a parallel conductor model and calculated [e.g., *Bourlange et al.*,

2003] from the LWD ring conductivity, σ_b, the conductivity of the samples, σ_r, and the interstitial fluid conductivity σ_{if}, as follows:

$$\phi_c = \frac{\sigma_b - \sigma_r}{\sigma_{if} - \sigma_r}. \qquad (14)$$

[33] For a sample conductivity of 0.69 S m⁻¹, a logging conductivity of 0.85 S m⁻¹ and an interstitial fluid conductivity of 4.45 S m⁻¹, all at 20°C, a fracture porosity of approximately 4% is estimated at a depth of 440 m. Below ~500 m to the bottom of the hole, the mud pressure was increased above the hydrostatic pressure to overpass difficult drilling conditions. High mud pressure may have caused the formation of tensile fractures or increased the dilation of pre-existing high-angle fractures, as observed on the resistivity images [*Kinoshita et al.*, 2009]. The corresponding resistivity anomaly in the LWD data below 500 m therefore cannot be considered representative of in situ conditions.

5. Discussion and Conclusion

[34] Here, we have shown that the estimation of porosity from resistivity using shaly sediment models is systematically improved when a distinction is made between the water bound to clay minerals and the interstitial porosity. Furthermore, the values of the correlation coefficients between model and sample data indicate that the interstitial porosity estimation is a valuable proxy for interstitial porosity when no direct measurements are available. The correction of interstitial porosity to account for swelling clay content appears to be useful for clarifying the lithological origin of several of the porosity anomalies observed, and more generally, for assessing the compaction state of the sediments. Also, several studies [*Doan et al.*, 2011; *Hashimoto et al.*, 2010], show the importance of using such a porosity when correlating water content with other physical properties (e.g., *P* wave velocity). However, this model should be tested in sediments with a higher range of cation exchange capacity, since the variations among the lithologies drilled in the Kumano transect are moderate, 0.05 to 0.3 mol kg⁻¹.

[35] We show that recent erosion locally offsets porosity-effective stress relationships. By comparing these porosity effective stress relationships with a reference curve, we estimated erosion of ~57 and ~105 m at the top of Sites C0004 and C0008, respectively. Erosion is observed in zones where the slope appears steeper than average in the cross

section of the accretionary wedge (Figure 2). At Sites C0004 and C0008, erosion coincides with regional sliding scars observed in the mega-splay fault area on the 3-D seismic box (Strasser et al., submitted manuscript, 2010). Some local steepening processes likely caused slope unstablility at these locations (Strasser et al., submitted manuscript, 2010). At Site C0006, movement on the frontal thrust is an obvious slope steepening mechanism. At Sites C0004 and C0008, the slip on the splay fault has been slow for the last 1 Ma [*Strasser et al.*, 2009], but the additional effect of a décollement ramp or duplex system may be considered.

[36] The porosity of the underthrust sediments at Site C0004 suggests that they possibly experienced some overpressuring during a past episode of faster slips along the splay fault, but that the pore pressure is now released to hydrostatic conditions. At Site C0006, results on the underthrust sequence are inconclusive, but the presence of sand layers with a large lateral extent in the underthrust sequence [*Moore et al.*, 2009] would favor rapid fluid escape during the loading of the sediments.

[37] Based on in situ measurements and measurements on cores, fracture dilatation due to overpressuring can be argued at Site C0001. In order to maintain any possible overpressure, permeability would need to be sufficiently low or the loading rate sufficiently high in order to develop pore pressures more rapidly than they dissipate by drainage. The permeability measured on cores at Site C0001 ranges between 1 to 3×10^{-18} m^2 for effective pressures spanning possible in situ conditions (0 to 5 MPa depending on the fluid pressure) (unpublished data by T. Reuschlé et al., 2010). The geochemical data did not provide conclusive evidence for pore water freshening which could indicate fluid flow at Site C0001 [*Kinoshita et al.*, 2009], although a diffuse upward flow rate of a fraction of mm yr^{-1} may still be compatible with the data. Thus, for low loading rates and the presumed high permeability of the sediments measured on cores it appears difficult to propose a model maintaining a high-pressure zone as a steady state feature. This is possibly an interesting target for monitoring.

Acknowledgments

References

Archie, G. E. (1942), The electrical resistivity log as an aid in determining some reservoir characteristics, *JPT J. Pet. Technol.*, 5, 1–8.

Bangs, N. L. B., G. K. Westbrook, J. W. Ladd, and P. Buhl (1990), Seismic velocities from the Barbados Ridge Complex: Indicators of high pore fluid pressures in an accretionary complex, *J. Geophys. Res.*, 95, 8767–8782, doi:10.1029/JB095iB06p08767.

Blum, P. (1997), Physical properties handbook: A guide to the shipboard measurement of physical properties of deep-sea cores (online), *Tech. Note 26*, Ocean Drill. Program, College Station, Tex. (Available at http://www-odp.tamu.edu/publications/tnotes/tn26/INDEX.HTM)

Bourlange, S., P. Henry, J. C. Moore, H. Mikada, and A. Klaus (2003), Fracture porosity in the decollement zone of Nankai accretionary wedge using Logging While Drilling resistivity data, *Earth Planet. Sci. Lett.*, 209, 103–112, doi:10.1016/S0012-821X(03)00082-7.

Bray, C. J., and D. E. Karig (1985), Porosity of sediments in accretionary prisms and some implications for dewatering processes, *J. Geophys. Res.*, 90, 768–778, doi:10.1029/JB090iB01p00768.

Brown, K. M., and B. Ransom (1996), Porosity corrections for smectite-rich sediments: Impact on studies of compaction, fluid generation, and tectonic history, *Geology*, 24, 843–846, doi:10.1130/0091-7613(1996)024<0843:PCFSRS>2.3.CO;2.

Bussian, A. E. (1983), Electrical conductance in a porous medium, *Geophysics*, 48(9), 1258–1268, doi:10.1190/1.1441549.

Chang, C., L. C. McNeill, J.C. Moore, W. Lin, M. Conin, and Y. Yamada (2010), In situ stress state in the Nankai accretionary wedge estimated from borehole wall failures, *Geochem. Geophys. Geosyst.*, 11, Q0AD04, doi:10.1029/2010GC003261.

Clavier, C., G. Coates, and J. Dumanoir (1984), Theoretical and experimental bases for the dual-water model for interpretation of shaly sands, *SPEJ Soc. Pet. Eng. J.*, 24(2), 153–168, doi:10.2118/6859-PA.

Colten-Bradley, V. A. (1987), Role of pressure in smectite dehydratation–Effects on geopressure and smectite to illite transformation, *AAPG Bull.*, 71, 1414–1427.

Dahlen, F. A. (1984), Noncohesive critical Coulomb wedges; an exact solution, *J. Geophys. Res.*, 89, 10,125–10,133, doi:10.1029/JB089iB12p10125.

Doan, M.-L., M. Conin, P. Henry, T. Wiersberg, D. Boutt, D. Buchs, D. Saffer, L. C. McNeill, and D. Cukur (2011), Quantification of free gas in the Kumano fore-arc basin detected from borehole physical properties: IODP NanTroSEIZE drilling Site C0009, *Geochem. Geophys. Geosyst.*, 12, Q0AD06, doi:10.1029/2010GC003284.

Glover, P. W. J., M. J. Hole, and J. Pous (2000), A modified Archie's law for two conducting phases, *Earth Planet. Sci. Lett.*, 180, 369–383, doi:10.1016/S0012-821X(00)00168-0.

Gordon, D. S., and P. B. Flemings (1998), Generation of overpressure and compaction-driven fluid flow in a Plio-

Pleistocene growth-faulted basin, Eugene Island 330, offshore Louisiana, *Basin Res.*, *10*, 177–196, doi:10.1046/j.1365-2117.1998.00052.x.

Hart, B. S., P. B. Flemmings, and A. Deshpande (1995), Porosity and pressure: Role of compaction disequilibrium in the development of geopressures in a Gulf Coast Pleistocene basin, *Geology*, *23*, 45–48, doi:10.1130/0091-7613(1995)023<0045:PAPROC>2.3.CO;2.

Hashimoto, Y., H. J. Tobin, and M. Knuth (2010), Velocity-porosity relationships for slope apron and accreted sediments in the Nankai Trough Seismogenic Zone Experiment, Integrated Ocean Drilling Program Expedition 315 Site C0001, *Geochem. Geophys. Geosyst.*, *11*, Q0AD05, doi:10.1029/2010GC003217.

Henry, P. (1997), Relationship between porosity, electrical conductivity and cation exchange capacity in Barbados wedge sediments, *Proc. Ocean Drill. Program Sci. Results*, *156*, 137–149.

Henry, P., and S. Bourlange (2004), Smectite and fluid budget at Nankai IODP sites derived from cation exchange capacity, *Earth Planet. Sci. Lett.*, *219*, 129–145, doi:10.1016/S0012-821X(03)00694-0.

Henry, P., S. Mazzotti, and X. Le Pichon (2001), Transient deformation of central Japan estimated by GPS. 1. Interseismic loading and subduction kinematics, *Earth Planet. Sci. Lett.*, *184*, 443–453, doi:10.1016/S0012-821X(00)00335-6.

Hubbert, M. K., and W. W. Rubey (1959), Role of fluid pressure in mechanics of overthrust faulting, *Geol. Soc. Am. Bull.*, *70*, 115–166, doi:10.1130/0016-7606(1959)70[115:ROFPIM]2.0.CO;2.

Karig, D. E. (1993), Reconsolidation tests and sonic velocity measurements of clay-rich sediments from the Nankai Trough, *Proc. Ocean Drill. Program Sci. Results*, *131*, 247–260.

Kinoshita, M., H. Tobin, J. Ashi, G. Kimura, S. Lallemant, E. J. Screaton, D. Curewitz, H. Masago, K. T. Moe, and the Expedition 314/315/316 Scientists (2009), *Proceedings of the Integrated Drilling Program Expeditions*, vol. 314/315/316, Integr. Ocean Drill. Program, Washington, D. C., doi:10.2204/iodp.proc.314315316.2009.

Le Pichon, X., P. Henry, and S. Lallemant (1993), Accretion and erosion in subduction zones: The role of fluids, *Annu. Rev. Earth Planet. Sci.*, *21*, 307–331, doi:10.1146/annurev.ea.21.050193.001515.

Leroy, P., and A. Revil (2004), A triple-layer model of the surface electrochemical properties of clay minerals, *J. Colloid Interface Sci.*, *270*, 371–380, doi:10.1016/j.jcis.2003.08.007.

Miyazaki, S., and K. Heki (2001), Crustal velocity field of southwest Japan: Subduction and arc-arc collision, *J. Geophys. Res.*, *106*, 4305–4326, doi:10.1029/2000JB900312.

Moore, J. C., and D. M. Saffer (2001), Updip limit of the seismogenic zone beneath the accretionary prism of southwest Japan: An effect of diagenetic to low grade metamorphic processes and increasing effective stress, *Geology*, *29*, 183–186, doi:10.1130/0091-7613(2001)029<0183:ULOTSZ>2.0.CO;2.

Moore, J. C., and P. Vrolijk (1992), Fluids in accretionary prisms, *Rev. Geophys.*, *30*, 113–135, doi:10.1029/92RG00201.

Moore, G. F., et al. (2001), *Proceedings of the Ocean Drilling Program, Initial Reports*, *190*, Ocean Drill. Program, College Station, Tex., doi:10.2973/odp.proc.ir.190.2001.

Moore, G. F., et al. (2009), Structural and seismic stratigraphic framework of the NanTroSEIZE Stage 1 transect, in *NanTroSEIZE Stage 1: Investigations of Seismogenesis,*

Nankai Trough, Japan, *Proc. Integr. Ocean Drill. Program*, *314/315/316*, doi:10.2204/iodp.proc.314315316.102.2009.

Orsini, L., and J. C. Remy (1976), Utilisation du chlorure de cobaltihexamine pour la détermination simultanée de la capacité d'échange et des bases échangeables des sols, *Sci. Sol*, *4*, 269–275.

Park, J.-O., T. Tsuru, S. Kodaira, P. R. Cummins, and Y. Kaneda (2002), Splay fault branching along the Nankai subduction zone, *Science*, *297*, 1157–1160, doi:10.1126/science.1074111.

Raimbourg, H., Y. Hamano, S. Saito, M. Kinoshita, and A. Kopf (2011), Acoustic and mechanical properties of Nankai accretionary prism core samples, *Geochem. Geophys. Geosyst.*, doi:10.1029/2010GC003169, in press.

Ransom, B., and H. C. Helgeson (1994), A chemical and thermodynamic model of dioctahedral 2:1 layer clay minerals in diagenetic processes: Regular solution representation of interlayer dehydratation in smectite, *Am. J. Sci.*, *294*, 449–484, doi:10.2475/ajs.294.4.449.

Revil, A., L. M. Cathles III, S. Losh, and J. A. Nunn (1998), Electrical conductivity in shaly sands with geophysical applications, *J. Geophys. Res.*, *103*, 23,925–23,936, doi:10.1029/98JB02125.

Rubey, W. W., and M. K. Hubbert (1959), Role of fluid pressure in mechanics of overthrust faulting, *Geol. Soc. Am. Bull.*, *70*, 167–206, doi:10.1130/0016-7606(1959)70[167:ROFPIM]2.0.CO;2.

Saffer, D. M., and B. A. Bekins (2006), An evaluation of factors influencing pore pressure in accretionary complexes: Implications for taper angle and wedge mechanics, *J. Geophys. Res.*, *111*, B04101, doi:10.1029/2005JB003990.

Scholz, C. H. (1998), Earthquakes and friction laws, *Nature*, *391*, 37–42, doi:10.1038/34097.

Screaton, E., D. M. Saffer, P. Henry, S. Hunze, and the Leg 190 Shipboard Scientific Party (2002), Porosity loss within the underthrust sediments of the Nankai accretionary complex: Implications for overpressures, *Geology*, *30*, 19–22, doi:10.1130/0091-7613(2002)030<0019:PLWTUS>2.0.CO;2.

Screaton, E., G. Kimura, D. Curewitz, G. Moore, and IODP Expeditions 314, 315, 316 Scientific Parties (2009), Interactions between deformation and fluids in the frontal thrust region of the NanTroSEIZE transect offshore the Kii Peninsula, Japan: Results from IODP Expedition 316 Sites C0006 and C0007, *Geochem. Geophys. Geosyst.*, *10*, Q0AD01, doi:10.1029/2009GC002713.

Sen, P. N., and R. Kan (1987), Electrolytic conduction in porous media with charges, *Phys. Rev. Lett.*, *58*, 778–780, doi:10.1103/PhysRevLett.58.778.

Seno, T., S. Stein, and A. E. Gripp (1993), A model for motion of the Philippine Sea plate consistent with NUVEL-1 and geological data, *J. Geophys. Res.*, *89*, 941–948.

Song, I., R. M. Skarbek, D. M. Saffer, and P. B. Flemings (2008), A comparison of compression behavior of mudrock core samples from the Nankai Margin, SW Japan and the Ursa Basin, Gulf of Mexico, *Eos Trans. AGU*, *89*(53), Fall Meet. Suppl., Abstract T31A-1985.

Strasser, M., et al. (2009), Origin and evolution of a splay fault in the Nankai accretionary prism, *Nat. Geosci.*, *2*, 648–652.

Underwood, M. B., and J. F. Steurer (2003). Composition and sources of clay from the trench slope and shallow accretionary prism of Nankai Trough (online), *Proc. Ocean Drill. Program Sci. Results*, *190/196*. (Available at http://www-odp.tamu.edu/publications/190196SR/206/206.htm)